Design and Analysis of the Integrated Motor Cooling System for Shaftless Propeller

ZHU HAO, JIN SHUANBAO, WANG DONG, WANG GONGBAO, AND HU PENGFEI

National Key Laboratory of Science and Technology on Vessel Integrated Power System, Naval University of Engineering, Wuhan 430033, China

Corresponding author: Jin Shuanbao (hjgcjin@163.com)

ABSTRACT In order to deal with the heat dissipation of the integrated permanent magnet motor for a certain shaftless propeller, this paper designs an automatic water-circulation cooling system. The cooling system involves two annular grooves on the inner wall of the duct before and after the blades, the two grooves are connected with the air-gap between the motor stator and rotor to form a cooling passage in which cooling water flows from the rear of the propeller to the front. The performance analysis of the cooling system is a multi-physics problem involving electromagnetic field, flow field, and temperature field. This study combines the finite element method and the finite volume method to simulate and analyze the multi-field coupling problem of the cooling system. Tests of the shaftless propeller prototype are used to prove that the coupling simulation model is accurate and the cooling system is practical. Additionally, the verified simulation model is applied to analyzing the influence of several key factors, such as air-gap flow rate, pouring sealant thermal conductivity, and stator sheath material, on the heat dissipation of the integrated motor. The study made in this paper can provide a reference for developing the same kind of devices.

INDEX TERMS Coupling simulation model, integrated motor, shaftless propeller, temperature field.

I. INTRODUCTION

The shaftless propeller is a new-type electric propulsion device that integrates the motor rotor with the propeller blades [1]. The blades can be directly driven by the rotating motor rotor, and this kind of propulsion device does not need the shafting and related supporting systems and accessories. With the rapid development of electric propulsion technology, the shaftless propeller characterized by high integration and modularization has come into being. Now it is playing an important role in the promotion of high power density, high propulsion efficiency, high maneuverability, and low radiation noise in the field of marine propulsion [2]–[5]. Unlike the traditional propulsion motors in the ship cabin, the shaftless propeller motor is integrated into the duct and installed outside the ship [6]. Due to the limitation of the space inside the duct, the motor should not be too large in volume, and its power density is high, and there is not enough space in the duct to install the cooling devices for the motor. Taking the advantage that the duct is directly immersed in the water,

The associate editor coordinating the review of this manuscript and approving it for publication was Md. Moinul Hossain.

the integrated motor usually uses an automatic water-circulation cooling system in engineering [7]–[11]. The system uses the air-gap of the motor as a water-cooled passage. While the propeller blades are rotating to generate thrust, the differential pressure between the inlet and outlet of the cooling passage is appearing, thereby providing power for water-circulation in the cooling passage, and bringing about heat dissipation and temperature reduction of the motor. The cooling system uses the water in the working environment as the cooling medium, so it has the advantages of high convective heat-transfer coefficient and high heat dissipation efficiency [12], [13]. Besides, the cooling system does not require auxiliary motor cooling devices, so it has the characteristics of simple and reliable structure, low power consumption, and low vibration noise.

Motor thermal analysis can be divided into two basic types: equivalent heat circuit and numerical methods, the numerical method includes the finite-element analysis (FEA) and the computational fluid dynamics (CFD) [14]. The heat dissipation analysis of the shaftless propeller motor involves the coupling of the electromagnetic field, flow field, and temperature field [15], [16]. Due to the special structure and the

small application rang of the shaftless propeller integrated motor, there are less published research papers on the analysis of its heat dissipation performance. Drouen *et al.* [15] and Wan [10] used the equivalent heat circuit method to analyze the multi-physics problem of the integrated motor. Although the equivalent heat circuit method has a fast calculation speed, it can only obtain the average temperature of each part in the motor, and the accuracy of the calculation results is low [14]. Xu *et al.* [11] used a three-dimensional (3D) CFD method based on the hydromechanics and heat transfer theories to analyze the temperature distribution of the integrated motor, but they used the air-gap flow rate as the boundary condition, and could not consider the effects of the blade rotation on the air-gap flow. The actual air-gap flow is complicated and turbulent due to the influence of the rotating blades. Liang *et al.* used a 3D coupled-field finite element method (FEM) to analyze the temperature distribution of the shaftless propeller motor [16], [17]. This method used the flow rate as the boundary condition of the air-gap inlet and proposed a multicomponent fluid method is to deal with the influence of rotating rotor upon the flow in the air-gap, but the effects of the rotating blades were ignored as well.

To solve the problem of heat dissipation from the integrated permanent magnet motor (IPMM) of a certain shaftless propeller, a whole system simulation model has been established for the coupling of the electromagnetic field, flow field, and temperature field of the motor. The hydrodynamic model of the propeller blades is directly coupled with the thermal model of the motor based on the CFD method. The velocity distribution in the air-gap is directly obtained by hydrodynamic calculation, so the influence of the rotating blades on the air-gap flow can be well considered. Then this model is used for numerical analysis, and experimental verification of this simulation model is carried out. Finally, several key factors affecting the cooling performance of the shaftless propeller motor have been analyzed, and some useful suggestions have been put forward.

II. AN OVERVIEW OF THE INTEGRATED MOTOR COOLING SYSTEM

According to the working principle of propellers, the shaftless propeller blades rotate in the duct and water are pushed out with high speed and high pressure, thrust is formed by the differential pressure between the inlet and outlet of the rotating blades [18]. The shaftless propeller has two annular open grooves on the inner wall of the duct, one is in front of the blades and the other is in the rear. The two grooves are connected with the air-gap between the stator and the rotor to form a cooling passage. The differential pressure produced by the rotating blades can force water to flow in the cooling passage from the rear of the propeller to the front, thus dissipating the heat produced by the motor. Fig. 1 is a schematic diagram of the main structure and cooling passage of the shaftless propeller. The motor stator is installed in the duct. The stator and the rotor are both covered with water-proof sheaths. Integrated with the propeller blades, the rotor
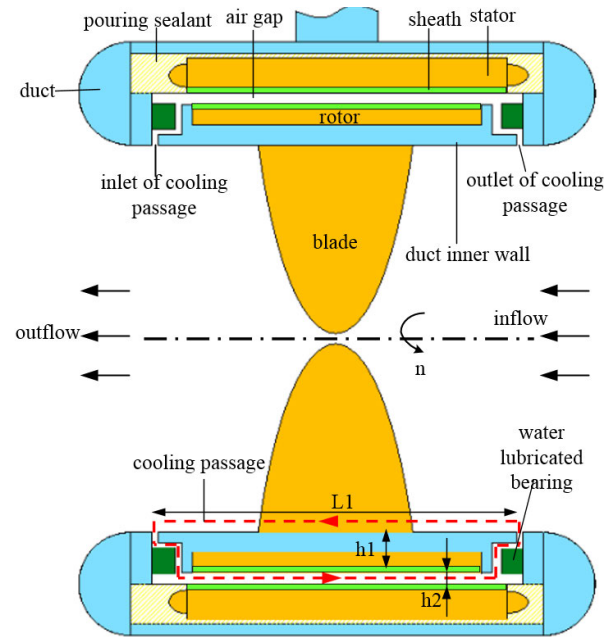
FIGURE 1. Schematic diagram of the structure and cooling passage of shaftless propeller.

can directly drive the blades to rotate and generate thrust. The thrust bearings and the support bearings are used to bear the vertical weight and the axial thrust load respectively, they are both lubricated by water. There are water-guiding grooves on the working face of the bearings. In addition, some other types of shaftless propellers still have the hub, which is fixed to the duct by the support ribs to support the rotating blades. The flow rate of water in the cooling passage is mainly determined by such factors as the hydrodynamic performance of the blades, thickness h1 and axial length L1 of the motor rotor, and height h2 of the air-gap.

III. MULTI-PHYSICS COUPLING SIMULATION AND EXPERIMENTAL VERIFICATION OF THE COOLING SYSTEM

In order to demonstrate the coupling performance of electromagnetic field, flow field and temperature field of the IPMM, the FEM is used to calculate the spatial distribution of electromagnetic loss of the motor, and a whole-system simulation model of the flow and temperature fields is established based on the finite volume method (FVM). This simulation model takes into account the influence of the rotating blades on the air-gap flow that is closely related to the motor heat dissipation performance, thus the actual turbulent flow in the air-gap is calculated to analyze the motor temperature distribution.

A. CALCULATION OF ELECTROMAGNETIC LOSS OF INTEGRATED MOTOR

Electromagnetic loss is the heat source for the calculation of the motor temperature field, so it is the basis of analyzing the heat dissipation of the motor. Whether the calculation
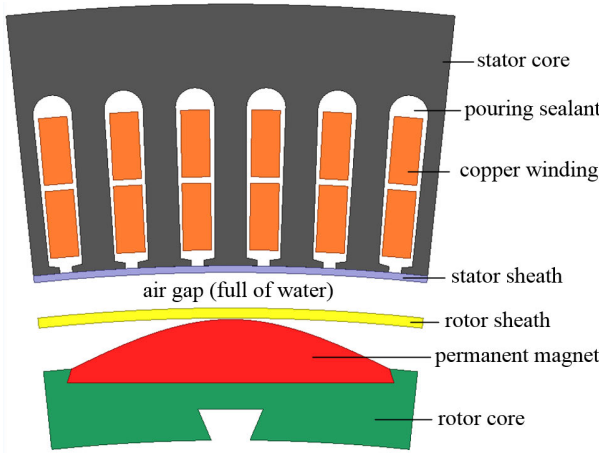
FIGURE 2. Schematic diagram of the layout and structure of shaftless propeller integrated motor.

FIGURE 3. Loss characteristic curves of the silicon steel.

of electromagnetic loss is accurate has a direct effect on the calculation of the motor temperature field.

The loss of the integrated motor comes from its stator and rotor. The stator loss includes: winding copper loss, iron loss, and waterproof metal sheath eddy current loss. The rotor loss includes waterproof sheath eddy current loss, iron loss, and permanent magnet eddy current loss. Fig. 2 shows the layout and structure of the designed shaftless propeller motor. The air-gap is not only the place where electromagnetic energy converts to mechanical energy but also acts as a cooling passage and accommodates itself to the stator and rotor sheath; therefore the air-gap height h2 of the motor is larger than that of a traditional motor of a similar size. When the motor is in operation, the fundamental magnetic motive force (MMF) of the stator rotates synchronously with the rotor, therefore the loss of the rotor is mainly caused by the stator high-order tooth harmonics and MMF harmonics. However, these high-order asynchronous harmonics can be effectively suppressed by the optimum design of the motor [19]–[21] and the large air-gap also can serve the function of filtering the high-order asynchronous harmonics. As a result, the rotor loss is very small (usually 1 to 2 in order of magnitude less than the stator loss). Additionally, when completely immersed in the water and rotating at high speed, the rotor is in excellent condition of heat dissipation. So its temperature rise can be ignored. Compared with the rotor, the stator has a large loss and is limited in heat dissipation. In this study, only the stator loss is taken into consideration so as to calculate the temperature field of the integrated motor.

1) COPPER LOSS OF THE STATOR

The stator copper loss is calculated according to Joule law. In the process of calculation, the fundamental alternating current (AC) additional copper loss needs to be considered. On condition that the current circulating around the shunt conductors of the single-turn coil is not taken into account, the coefficient added to the fundamental AC resistance of the winding in the slot can be calculated according to the classic
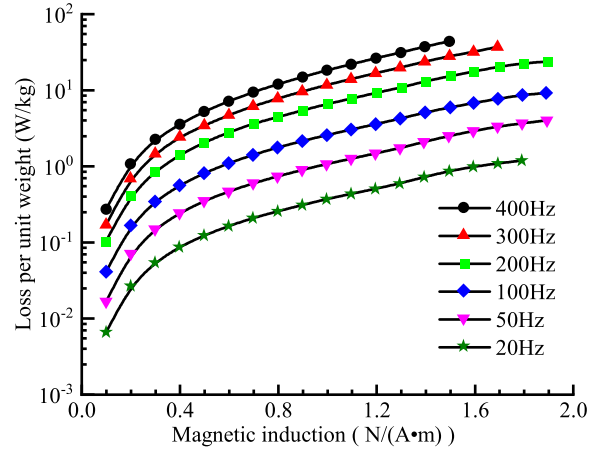
analytical formula [22]:

$$k_{slot} = \left(\frac{\mu_0 \cdot \pi \cdot f_1 \cdot m \cdot b}{3 \cdot \rho_{cu} \cdot b_{s2}} \right) \times a^4 \qquad (1)$$

where f_1 is the electric fundamental frequency (Hz); m is the total number of strands in the slot in terms of height; b is the copper width (m) in the slot; b_{s2} is the slot width (m); ρ_{cu} is the copper resistivity ($\Omega \cdot m$); a is the height of each copper wire (m). Under the rated condition, it is possible to obtain the increased coefficient of resistance of the windings in the slot, which is 0.83%, and the increased coefficient of resistance of the entire phase winding, which is 0.44%, by substituting the motor winding parameters into (1). According to the calculated DC resistance and the increased coefficient k_{slot} of AC resistance, the total AC loss of the copper winding under the rated condition can be calculated.

2) STATOR IRON LOSS

The stator iron loss is calculated according to the iron loss model based on the loss characteristics of the silicon steel sheet [23], [24]. According to the loss characteristic curves of the measured loss of the silicon steel sheet in Fig. 3, the iron loss model is expressed as follows:

$$P_v = K_h f B_m^2 + K_c f^2 B_m^2 + K_e f^{1.5} B_m^{1.5} \qquad (2)$$

where $K_h = 151.92$, which is the hysteresis iron loss coefficient; $K_c = 0.52582$, which is the eddy iron loss coefficient; $K_e = 0$, which is the additional iron loss coefficient; f is the alternating frequency of magnetic density (Hz); B_m is the magnetic density of the silicon steel sheet (N/(A·m)); the unit of iron loss is W/kg.

3) EDDY CURRENT LOSS OF THE STATOR SHEATH

The two-dimensional (2D) FEM cannot deal with the end effect of the motor, and the sheath eddy current path for calculation is small. As a result, the calculated eddy current loss of the stator sheath is greater than that in the practical situation. For this reason, it is necessary to establish a 3D finite element model to calculate the eddy current loss. The 3D model is shown in Fig. 4. The distribution of the eddy
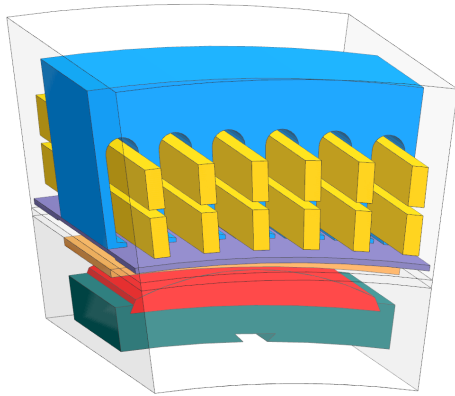
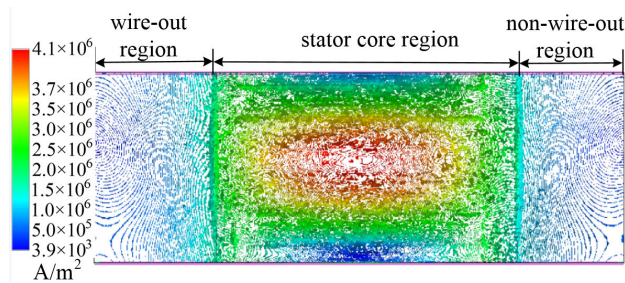**FIGURE 4.** The 3D model for calculating the sheath eddy current loss.

FIGURE 5. Distribution of eddy current density of the sheath.

TABLE 1. Distribution of electromagnetic loss of the motor under the rated condition.

Region	Wire-out region	Core region	Non-wire-out region	Total
Copper loss coefficient %	0.92	1.76	0.88	3.56
Iron loss coefficient %	-	0.38	-	0.38
Eddy current loss coefficient %	0.78	6.93	0.64	8.35

current density of the sheath under the rated condition is obtained from calculation, as shown in Fig.5.

The electromagnetic losses of different parts of the motor under the rated condition are listed in Table 1. The motor input power is about 28 kW at the rated speed of 500 rpm. The loss coefficient C_L in the table is calculated by

$$C_L = P_L/P_M \tag{3}$$

where P_L is the calculated value of loss (W) and P_M is the motor input power (W).

B. MULTI-PHYSICS COUPLING CALCULATION AND EXPERIMENTAL VERIFICATION

1) INTRODUCTION OF THE 3D SIMULATION MODEL

The motor loss distribution obtained from the electromagnetic calculation above is used as the energy source of the control equations of the fluid and heat transfer, the viscous flow field and temperature field of the shaftless propeller are solved by use of the ANSYS CFX program based on the central node control and the FVM. The shear stress
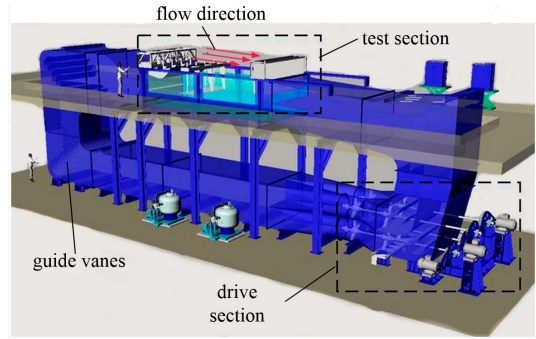
**(a) The test platform for shaftless propeller**
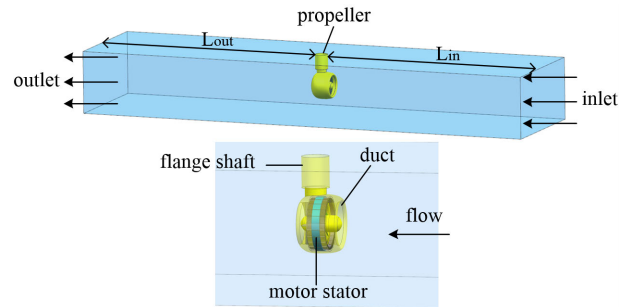
(b) The 3D simulation model for shaftless propeller

FIGURE 6. The test platform and the 3D simulation model for shaftless propeller.

transport (SST) turbulence model is adopted to compute the Reynolds stresses. The SST model combines the k-ε turbulence model with the k-ω model together, it can better simulate the viscous laminar flow [25]. The flow in the near-wall region is treated by the automatic wall functions. The rotation field of the impeller blades is solved by the multiple frames of reference (MFR) method. Heat transfer in the whole model is calculated by the thermal model.

In order to facilitate the comparison between the calculation and the test results, the 3D simulation model for the performance calculation of the shaftless propeller is established according to the boundaries of the test platform (a circulating water channel), as shown in Fig. 6. The inlet and the outlet of the calculation domain use the velocity and the pressure boundary conditions respectively. The distribution of the inlet velocity and outlet pressure can be obtained by test measurements. The length of the inlet section (L_{in}) and the outlet section (L_{out}) of the calculation domain both are 15 times the impeller diameter (15D). The calculation domain of the impeller and the motor rotor is a rotational domain, and the rest are static domains. The stator of the motor is a static solid domain. Since the whole stator is wrapped in the duct, the condition for transmitting heat through the internal structure of the duct is relatively poor. Therefore, the outer surface of the stator is set as an adiabatic wall except for the part in contact with water. The part in contact with the cooling water in the air-gap is set as a fluid-solid interface for heat exchange, and its heat transfer coefficient can be obtained through iteration of fluid and heat transfer equations.
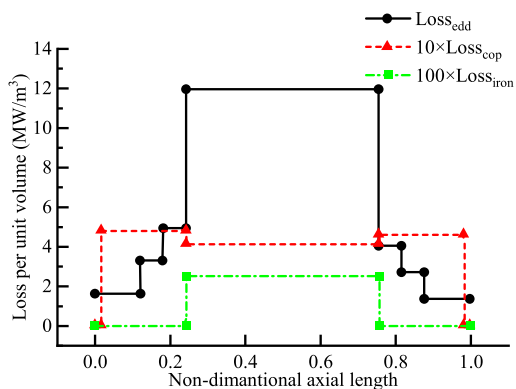
FIGURE 7. Distribution of the loss per unit volume along the axial direction of the motor.

According to the loss distribution from the electromagnetic calculation above, the loss per unit volume of different parts of the stator can be obtained and loaded as an energy source term into the corresponding solid calculation domain for temperature field simulation. Fig. 7 shows the distribution of the eddy current loss ($Loss_{edd}$), copper loss ($Loss_{cop}$), iron loss ($Loss_{iron}$) per unit volume along the axial direction of the motor. In order to facilitate the observation of the distribution curves, the copper and iron losses in the figure are magnified 10 and 100 times, respectively.

2) GRID OF THE MODEL

The hexahedral structured grid is used to discretize the entire calculation domain of the flow field. The grids in the flow field and on the propeller surface are shown in Fig. 8(a) and 8(b). For the solid calculation domain of the motor stator, the core region is discretized by hexahedral structured grids, as shown in Fig. 8(c). The stator ends are discretized by tetrahedral unstructured grids. In order to eliminate the calculation errors caused by the number of grids, this paper uses six kinds of grids of different densities to calculate the hydrodynamic performance of the propeller under the rated condition. The total numbers of the grid nodes in the domain with different grid densities are 5.7×10^6, 10.5×10^6, 14.7×10^6, 19.4×10^6, 23.3×10^6, 35.6×10^6, respectively. The thrust coefficients of the propeller are calculated and shown in Fig. 9. As the total number of grids in the fluid domain increases, the thrust coefficient decreases first and then remains nearly unchanged. In order to ensure the calculation accuracy and reduce the calculation cost, the paper finally determines that the total number of grid nodes of the domain is about 19.4×10^6.
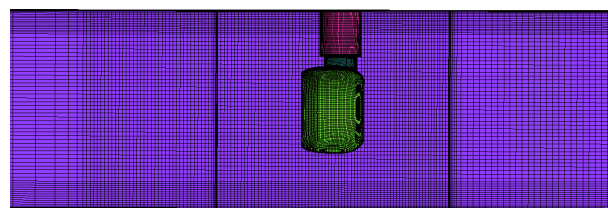
The thrust coefficient K_T in this paper is defined as follows:

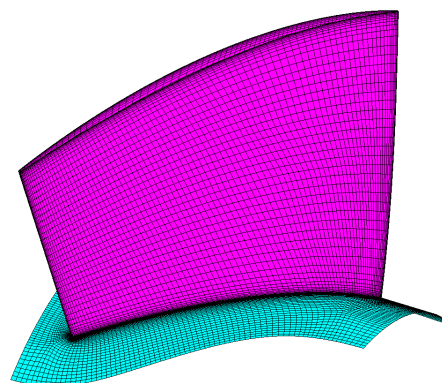$$K_T = T / \left(\rho n^2 D^4 \right) \quad (4)$$

where T is the total thrust of the propeller (N), n is the motor rotational speed (rpm), D is the impeller diameter (m).
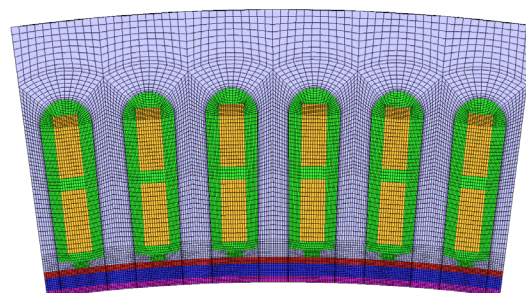
3) TEST OF THE SHAFTLESS PROPELLER

In order to verify the accuracy of the coupled simulation model and the effectiveness of the cooling system, the test

(a) Grids in the flow field

(b) Grids on the impeller blade

(c) Grids in the stator

FIGURE 8. Grids of the simulation model.

of the hydrodynamic performance and the motor temperature rise of the shaftless propeller prototype were carried out in the circulating water channel of Shanghai Jiao Tong University (SJTU). The 3D geometric model of the channel is shown in Fig. 6(a). The total length of the channel is about 27m, and the test section size is 8.0m (length) $\times$3.0m (width) $\times$1.6m (height) [26]. Fig. 10 shows the test prototype of the shaftless propeller in the channel. The upper part of the propeller is the flange shaft. A strain force-measuring sensor is installed on the flange shaft and used to measure the total thrust produced by the propeller. The temperature in the stator is measured by a thermal resistor PT100 installed in the copper winding. The resistance of the thermal resistor is proportional to the change in temperature. A pitot tube and a differential gage are installed upstream of the test section to measure the inflow velocity of the propeller. Before the tests, the sensitivity and the zero points of each measurement component are checked. During the tests, the inflow velocity of the prototype
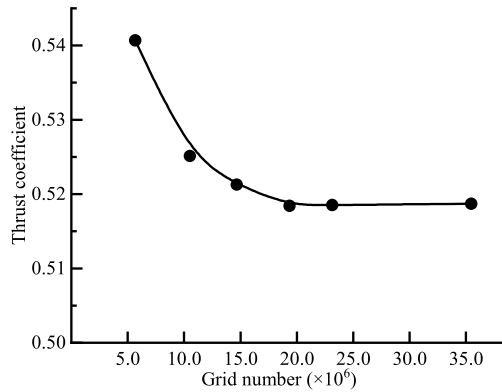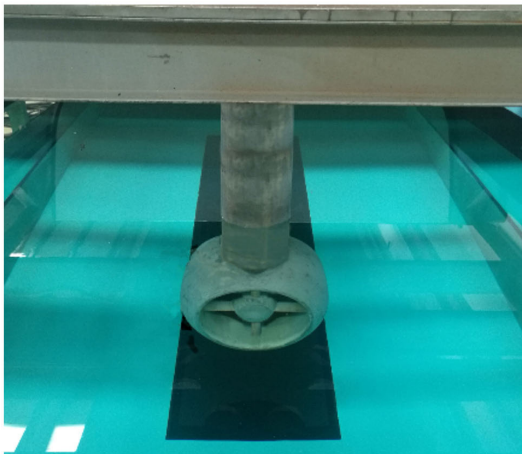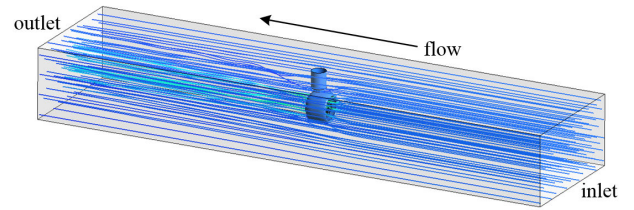
FIGURE 9. Grid independence analysis.

FIGURE 10. The shaftless propeller test prototype in the circulating water channel.

(a) Streamline distribution in the test section

(b) Streamline distribution inside and outside the shaftless propeller duct, and in the air-gap

FIGURE 11. Streamline distribution in the test section and in the air-gap.

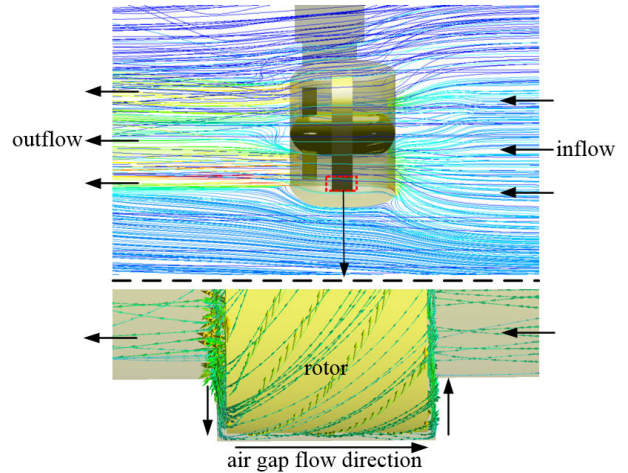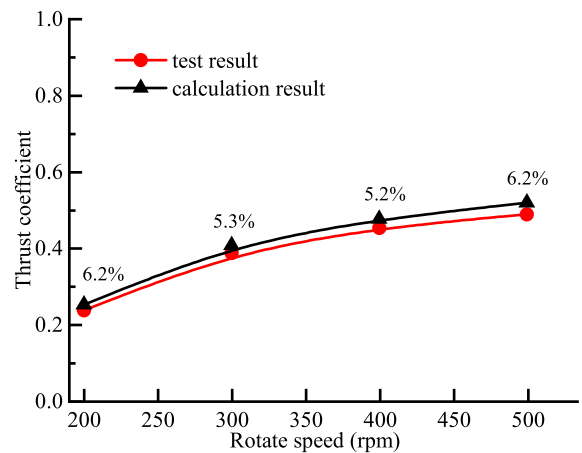**FIGURE 12. Comparison between the calculation and test results of thrust coefficients.**

is kept constant, and the total thrust of the propeller and the motor temperature rise at different speeds are measured.

4) COMPARISON BETWEEN THE CALCULATION AND TEST RESULTS

Fig. 11 (a) shows the streamline distribution in the test section of the circulating water channel after steady hydrodynamic simulation. Fig. 11 (b) shows the detailed streamline distribution inside and outside the propeller duct, and in the air-gap. It can be seen that the streamlines in the air-gap are neither uniform nor in a straight line, they are disordered and have a large velocity component in the circumferential direction, these are caused by the rotation of the blades. As shown in Fig. 12, a comparison is made between the calculation and test results of thrust coefficients of the prototype operating at different speeds. The error percentages of the calculation results compared with test results are also listed in Fig. 12. From the comparison, it can be seen that the thrust calculation results are higher than the test results, but the error between them is not more than 6.2%. The main reason that calculation results are higher is that the numerical simulation model is ideal, and the model surfaces are perfectly smooth, but the actual test prototype has manufacturing errors, and the blades and the duct have a certain roughness on their surfaces.

The calculation errors meet the requirements in engineering, so the hydrodynamic simulation model is proved to be accurate.

The thermal conductivity of the main components of the permanent magnet propulsion motor is shown in Table 2. The simulation results of the prototype temperature field are shown in Fig. 13. The result indicates that, under the condition of normal temperature and rated speed, the highest temperature of the stator appears at the end of the titanium alloy sheath, reaching 67.1 °C, the highest temperature of the

TABLE 2. Thermal conductivity of main components of the motor.

Name	Thermal conductivity W/(m·K)
Sheath (titanium alloy)	7
Pouring sealant	0.5
Copper	380
Silicon steel sheet	Radial: 20 Axial: 5

measuring point 1 in the stator slot is 34.9 °C, the highest temperature of the measuring point 2 at the end of copper winding is 37.9 °C. All the results are lower than the maximum limiting temperature specified by the H-class insulation level. The comparison of the test results with the calculated results of temperature of the shaftless propeller prototype is shown in Table 3, which indicates that the largest difference between them is less than 2 °C. This fully confirms that the cooling system of the motor is effective and the coupling simulation model of the motor temperature field is accurate.

IV. ANALYSIS OF SEVERAL FACTORS AFFECTING HEAT DISSIPATION OF THE MOTOR

Based on the verified coupling simulation model above, a simulation analysis has been made of several key factors affecting the heat dissipation of the motor, such as air-gap flow rate, thermal conductivity of the stator pouring sealant, and stator sheath material.

A. INFLUENCE OF AIR-GAP FLOW RATE ON HEAT DISSIPATION

The air-gap is a passage of the coupled electromagnetic, hydrodynamic, and temperature fields of the shaftless propeller. The air-gap flow is affected by factors such as blade hydrodynamic performance, rotor size, and air-gap size. According to the qualitative analysis, the air-gap flow rate increases with a rise in the blade hydrodynamic performance and in the air-gap height h_2, and with a decrease in the rotor thickness h_1 and its length L_1. However, the hydrodynamic loss caused by the air-gap flow rate also increases. Therefore, the relationship between the internal temperature of the motor and the air-gap flow rate needs to be analyzed so as to be used as the basis representing a compromise of the motor temperature and the propeller hydrodynamic efficiency. To this end, changes in the temperature field are analyzed by changing the air-gap flow rate under the condition of keeping other parameters constant. The calculated results are shown in Fig. 14. The air-gap flow rate is about 15 kg/s in the primary design for cooling system of the shaftless prototype. Now, the flow rate of 25 kg/s represents an excellent cooling condition, while the flow rate of 0.5 kg/s represents a very harsh condition in which the air-gap can be blocked. It is obvious that, even under the worst condition, the stator temperature is up to 93.5 °C, but lower than the limited temperature of 180 °C.
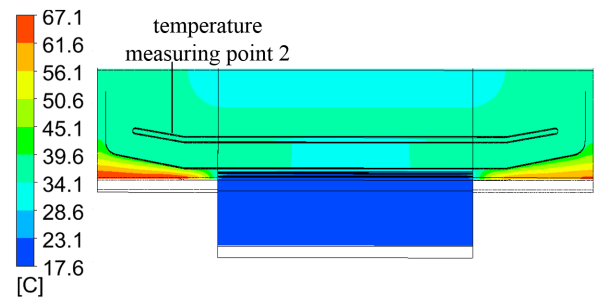
The above results show that the air-gap flow rate has not a significant effect on the heat dissipation of the shaftless propeller motor. The reasons are that the cooling system mainly depends on the air-gap flow to transfer heat, the area
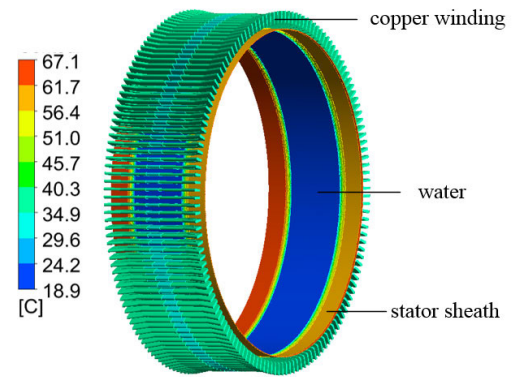
(a) Temperature distribution inside the whole stator
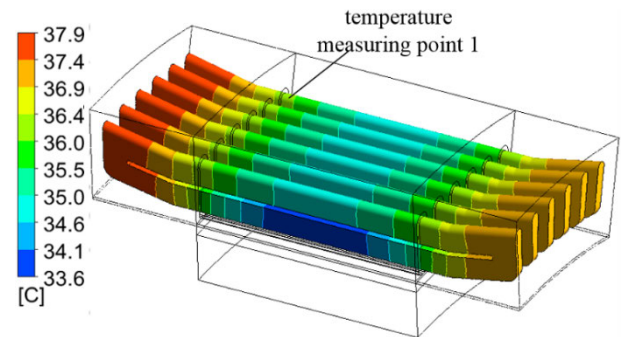
(b) Temperature distribution on the winding in a single pole

(c) Temperature distribution in the longitudinal section of the motor

FIGURE 13. Simulation results of temperature of the shaftless propeller motor.

TABLE 3. Comparison between the calculation and test results of motor temperature.

Measuring position	Test results °C	Calculation results °C
Point 1 (in the slot)	33.5	34.9
Point 2 (winding end)	36.9	37.9

of air-gap for heat transfer is basically unchanged, and the factors affecting heat dissipation are the temperature gradient and heat transfer coefficient which is positively correlated with the flow velocity in the air-gap. As shown in Table 4, the flow velocity in the air-gap is mainly determined by the circumferential velocity, the axial flow velocity is much less than the circumferential flow velocity. In other words, the axial flow velocity calculated according to the air-gap
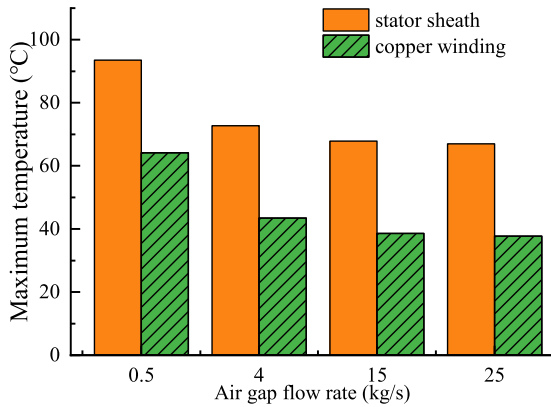
FIGURE 14. The maximum temperature of motor sheath and copper winding in the case of different air-gap flow rates.

TABLE 4. Resultant velocity in the air-gap with different flow rates.

Flow rate	Axial velocity	Circumferential velocity	Resultant velocity
kg/s	m/s	m/s	m/s
0.5	0.072	13.1	13.100
4	0.576	13.1	13.113
15	2.160	13.1	13.277
25	3.600	13.1	13.586

flow rate has a relatively small effect on heat transfer of the motor. When there is a certain steady mass flow rate in the air-gap (not less than 4kg/s), the change of the air-gap flow rate has no significant effect on heat dissipation. However, when the mass flow in the air-gap is almost blocked(less than 0.5kg/s) and the axial flow velocity is greatly reduced, the water temperature in the air-gap rises, and the temperature gradient between the stator and the air-gap water is reduced, as a result, heat produced by the motor cannot be taken away in time and the stator temperature has a significant rise.

B. INFLUENCE OF THERMAL CONDUCTIVITY OF POURING SEALANT ON HEAT DISSIPATION

As an immersed motor, the shaftless propeller IPMM depends on the sheath and pouring sealant to seal and insulate its stator and rotor. Also, the quality of both the sheath and pouring sealant as the main media of heat transmission has a direct effect on heat dissipation of the motor. When the other parameters remain unchanged, the changes of maximum temperature of the sheath and the copper winding can be calculated by changing the thermal conductivity of the pouring sealant, as shown in Fig. 15. The calculated results show that the thermal conductivity of the pouring sealant has an obvious effect on the motor heat dissipation. When the thermal conductivity is less than 0.5 W/(m·K), the maximum temperature of the sheath is close to 90 °C. For further improvement on the safety and reliability of the motor, this paper makes a recommendation that a kind of pouring sealant whose thermal conductivity is higher than 1 W/(m·K) should be used, and the maximum temperature of the motor should be kept in a lower range.
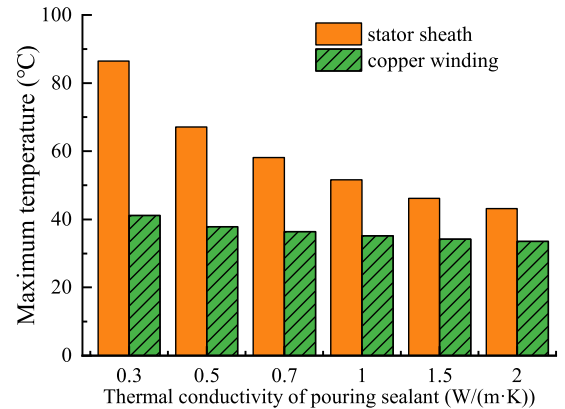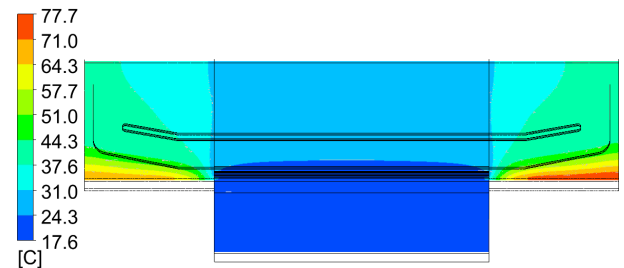

FIGURE 15. The maximum temperature of motor sheath and copper winding in the case of different thermal conductivity of pouring sealant.

(a) Temperature distribution on the longitudinal profile of the motor with Hastelloy sheath
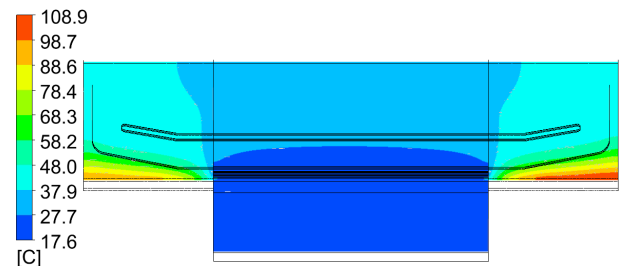
(b) Temperature distribution on the longitudinal profile of the motor with Stainless steel sheath
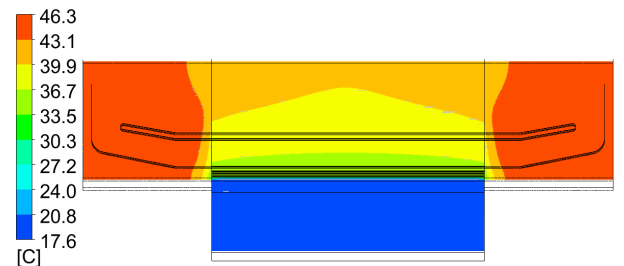
(c) Temperature distribution on the longitudinal profile of the motor with FRP sheath

FIGURE 16. Temperature distribution on the longitudinal profiles of the motors with the sheath of different material.

C. INFLUENCE OF SHEATH MATERIAL ON HEAT DISSIPATION

The sheath is the only component in the stator that is directly in contact with the cooling water. Its thermal conductivity has

TABLE 5. Thermal conductivity and electrical resistivity of four kinds of sheath materials.

Material	Resistivity (μΩ·m)	Thermal conductivity (W/m·K)
Titanium alloy	1.7	7
Hastelloy	1.25	10.2
Stainless steel	0.7	15.9
FRP	Non-conducting	0.5

TABLE 6. Eddy current loss coefficients of the sheaths made of different materials.

Material	M1	M2	M3	M4
Eddy current loss coefficient (%)	8.354	11.454	20.454	0.000

M1 represents titanium alloy, M2 represents Hastelloy, M3 represents stainless steel, and M4 represents FRP (fiber reinforced plastics).

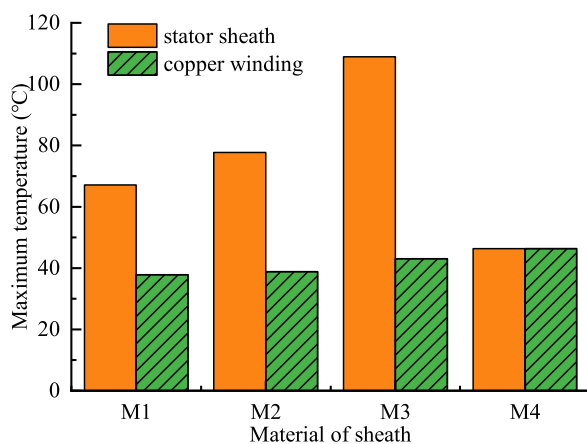**FIGURE 17.** The maximum temperature of motor sheath and copper winding in the case of different sheath materials.

an immediate influence on the heat dissipation of the motor. Moreover, the sheath is an important heat source because its own conductivity brings about eddy current loss. For this reason, in choosing a kind of sheath material for the motor, it is necessary to fully consider its thermal conductivity and electrical resistivity. The sheath of the shaftless propeller prototype is made of titanium alloy. Another three typical kinds of sheath materials, such as Hastelloy, stainless steel and fiber-reinforced plastics (FRP), are selected to analyze their effects on the heat dissipation of the motor. The thermal conductivity and electrical resistivity of the above four kinds of materials are listed in Table 5. The eddy current loss coefficients of different sheaths obtained from calculation are listed in Table 6. The temperature distribution on the longitudinal profile of the stator is shown in Fig. 16. The maximum temperature of the sheaths and the copper winding are shown in Fig. 17. It can be seen from Fig. 16 that the maximum temperature of the stator appears at the sheath end, because only the middle part of the sheath is in contact with cooling water in the air-gap, while the sheath end acts as a supporting part and so the cooling water cannot pass, resulting in heat concentration on the sheath end. According to Fig. 17, the sheath of FRP is the best in heat

dissipation performance, which is because FRP is not conductive and does not generate eddy current loss, and the less heat generated inside the stator by the currently-used motor with small power can be transferred to water in time. But if there is an increase in power of the motor, the heat generated inside the stator will increase quickly. When it exceeds the heat transfer capacity of the FRP sheath, the temperature inside the sheath and the stator will rise sharply. In order to prevent the temperature of the FRP sheath from reaching its limited value 80°C, it is better to select titanium alloy for the stator sheath or take some measures to improve the thermal conductivity of FRP. For example, the thermal conductivity of FRP can be improved by adding some metal powder.

V. CONCLUSION

The motor of shaftless propeller is integrated with the duct and arranged outside the cabin, which results in a significant change in the working environment of the motor. Compared with the traditional propulsion motor, the shaftless propeller integrated motor has characteristics of complex structure, high integration, high power density and components coupling. Aiming at the heat dissipation of the shaftless propeller motor, this paper has fulfilled the design of the automatic water-circulation cooling system, this system relies on the rotation of propeller blades for power. A multi-physics coupling simulation model of electromagnetic field, flow field, and temperature filed of the whole system is established. The test results of the shaftless propeller prototype show that the cooling system and the simulation model are feasible and effective. Based on the verified model, several important factors affecting the heat dissipation of the shaftless propeller are analyzed. The conclusion is given as follows:

1) For a high-speed shaftless propeller, the cooling water flow rate has no significant influence on the heat dissipation of the motor. The height of the air-gap can be appropriately reduced to decrease the air-gap flow rate, this can not only improve the hydrodynamic efficiency of the propeller but also keep the maximum temperature of the integrated motor in the limited range.

2) The sheath end of the motor stator is the place where heat is easy to accumulate. Therefore, in designing the shaftless propeller, it is necessary to full consider the performance of heat dissipation of the sheath and optimize the design, for example, selecting suitable sheath materials of high thermal conductivity and resistivity, expanding the area of contact between the sheath and the cooling water, and adding a flow passage to the sheath end of the stator. In addition, the thermal conductivity of the pouring sealant affects the heat dissipation of the motor significantly, so it is better to use a material with high thermal conductivity and fine sealability as pouring sealant of the motor.

REFERENCES

[1] B.-W. Song, Y.-J. Wang, and W.-L. Tian, "Open water performance comparison between hub-type and hubless rim driven thrusters based on CFD method," *Ocean Eng.*, vol. 103, pp. 55–63, Jul. 2015.

[2] X. Yan, X. Liang, W. Ouyang, Z. Liu, B. Liu, and J. Lan, "A review of progress and applications of ship shaft-less rim-driven thrusters," *Ocean Eng.*, vol. 144, pp. 142–156, Nov. 2017.

[3] H.-G. Wang, "Study of vibration isolation and noise reduction technology in US nuclear submarine propulsion system," *Ship Sci. Technol.*, vol. 35, no. 7, pp. 149–153, 2013.

[4] L. Drouen, J. F. Charpentier, F. Hauville, E. Semail, and S. Clenet, "A coupled electromagnetic/hydrodynamic model for the design of an integrated rim-driven naval propulsion system," in *Proc. ElectrIMACS*, Montreal, QC, Canada, Jun. 2008, pp. 1–6.

[5] M. Lea, D. Thompson, B. Van Blarcom, J. Eaton, J. Friesch, and J. Richards, "Scale model testing of a commercial rim-driven propulsor pod," *J. Ship Prod.*, vol. 19, no. 2, pp. 121–130, 2003.

[6] M. Weiming, "Electromechanical power conversion technologies in vessel integrated power system," *J. Elect. Eng.*, vol. 10, no. 4, pp. 3–10, 2015.

[7] T. Tang and C. Han, *Ship Electric Propulsion System*. Beijing, China: Mechanical Industry Press, 2015, pp. 123–135.

[8] W. Liu and Y. Hu, "Analysis of construction principle and characteristics of pump-jet for underwater integrated motor propulsor," *Torpedo Technol.*, vol. 15, no. 6, pp. 5–8, 2007.

[9] Z. Wang, "ABB exquisitely developing azipod CZ deep water drilling propulsion solution," *Ship Economy Trade*, vol. 1, pp. 44–45, 2010.

[10] L. Wan, "The thermal design of propulsion motor on IMP," M.S. thesis, China Ship Res. Inst., Beijing, China, 2018.

[11] S. Xu, H. Wang, and G. Gu, "Analysis of temperature distribution for the electric generator in rim-driven marine current power system," in *Proc. Int. Conf. Elect. Mach. Syst. (ICEMS)*, Oct. 2013, pp. 843–846.

[12] W. He, "Water cooling system design and temperature analysis of PMSM in electrical vehicle," M.S. thesis, Dept. Elect. Eng., Zhejiang Uni., Hangzhou, China, 2013.

[13] M. Polikarpova, "Liquid cooling solutions for rotating permanent magnet synchronous machines," Ph.D. dissertation, Dept. Mech. Eng., Lappeenranta Univ. Technol., Lappeenranta, Finland, 2014.

[14] A. Boglietti, A. Cavagnino, D. Staton, M. Shanel, M. Mueller, and C. Mejuto, "Evolution and modern approaches for thermal analysis of electrical machines," *IEEE Trans. Ind. Electron.*, vol. 56, no. 3, pp. 871–882, Mar. 2009.

[15] L. Drouen, J. F. Charpentier, E. Semail, and S. Clenet, "A global approach for the design of a rim-driven marine turbine generator for sail boat," in *Proc. 20th Int. Conf. Elect. Mach. (ICEM)*, Sep. 2012, pp. 549–555.

[16] J. Liang, X. Zhang, M. Qiao, P. Zhu, W. Cai, Y. Xia, and G. Li, "Optimal design and multifield coupling analysis of propelling motor used in a novel integrated motor propeller," *IEEE Trans. Magn.*, vol. 49, no. 12, pp. 5742–5748, Dec. 2013.

[17] J. Liang, X. Zhang, M. Qiao, and G. Li, "Multifield coupling analysis of integrated motor propulsor," *TELKOMNIKA Indones. J. Electr. Eng.*, vol. 10, no. 7, pp. 1897–1903, 2012.

[18] Z. Sheng and Y. Liu, *Ship Theory*. Shanghai, China: Shanghai Jiaotong Univ. Press, 2003, pp. 17–31.

[19] Z. Shi, X. Sun, Y. Cai, Z. Yang, G. Lei, Y. Guo, and J. Zhu, "Torque analysis and dynamic performance improvement of a PMSM for EVs by skew angle optimization," *IEEE Trans. Appl. Supercond.*, vol. 29, no. 2, pp. 1–5, Mar. 2019.

[20] X. Sun, Z. Shi, G. Lei, Y. Guo, and J. Zhu, "Analysis and design optimization of a permanent magnet synchronous motor for a campus patrol electric vehicle," *IEEE Trans. Veh. Technol.*, vol. 68, no. 11, pp. 10535–10544, Nov. 2019.

[21] X. Sun, Z. Jin, S. Wang, Z. Yang, K. Li, Y. Fan, and L. Chen, "Performance improvement of torque and suspension force for a novel five-phase BFSPM machine for flywheel energy storage systems," *IEEE Trans. Appl. Supercond.*, vol. 29, no. 2, pp. 1–5, Mar. 2019, Art. no. 0601505.

[22] S. Chen, *Motor Design*. Beijing, China: Mechanical Industry Press, 2000.

[23] X. Sun, Y. Shen, S. Wang, G. Lei, Z. Yang, and S. Han, "Core losses analysis of a novel 16/10 segmented rotor switched reluctance BSG motor for HEVs using nonlinear lumped parameter equivalent circuit model," *IEEE/ASME Trans. Mechatronics*, vol. 23, no. 2, pp. 747–757, Apr. 2018.

[24] H. Nam, K.-H. Ha, J.-J. Lee, J.-P. Hong, and G.-H. Kang, "A study on iron loss analysis method considering the harmonics of the flux density waveform using iron loss curves tested on Epstein samples," *IEEE Trans. Magn.*, vol. 39, no. 3, pp. 1472–1475, May 2003.

[25] G. Lloyd and A. Espanoles, "Best practice guidelines for marine applications of computational fluid dynamics," WS Atkins Consultants Members NSC, MARNET-CFD Thematic Netw., London, U.K., Tech. Rep., 2002, pp. 37–48.

[26] J. Li, "CFD application in design of wind tunnel-circulating water channel," M.S. thesis, Dept. Naval Archit. Ocean Eng., Shanghai Jiao Tong Uni., Shanghai, China, 2012.

ZHU HAO is currently pursuing the Ph.D. degree in electrical engineering with the Naval University of Engineering, Wuhan. His current research interests include propeller design and hydrodynamics.

JIN SHUANBAO received the Ph.D. degree in marine engine engineering from the Naval University of Engineering, Wuhan, in 2013. He is currently an Associate Researcher with the Naval University of Engineering. His current research interests include electric propulsion, integrated motor propeller design, and hydrodynamics.

WANG DONG received the Ph.D. degree in electrical engineering from the Naval University of Engineering, Wuhan, in 2007. He is currently a Professor and a Supervisor for doctoral candidates with the Naval University of Engineering. His current research interests include electric propulsion and integrated power generation systems.

WANG GONGBAO received the Ph.D. degree in electrical engineering from the Naval University of Engineering, Wuhan, in 2006. He is currently a Professor and a Supervisor for doctoral candidates with the Naval University of Engineering. His current research interests include wavelet analysis, neural network, and electrical power systems.

HU PENGFEI is currently pursuing the Ph.D. degree in electrical engineering with the Naval University of Engineering, Wuhan. His current research interests include power integration and integrated motor design.

• • •